J. Fluid Mech. (2000), *vol.* 425, *pp.* 31–53. Printed in the United Kingdom

Oscillatory flow of droplets in capillary tubes. Part 1. Straight tubes

By D. R. GRAHAM AND J. J. L. HIGDON

Department of Chemical Engineering, University of Illinois, Urbana, IL 61801, USA

(Received 25 June 1999 and in revised form 29 June 2000)

The motion of fluid droplets in capillary tubes subject to the action of a mean pressure gradient and an oscillatory body force is studied via numerical computations. The effects of the oscillatory forcing on the bulk flow rate and on the droplet velocity are evaluated, and results are presented for a range of forcing conditions, fluid properties and drop sizes. For large droplets (whose undeformed diameter exceeds that of the capillary tube), significant enhancement in the bulk flow rate is observed when the drop capillary number is small and the oscillatory forcing is strong. The enhancement is associated with increased droplet deformation in the presence of oscillatory forcing. The dependence of the flow enhancement on the amplitude, frequency and waveform of the oscillatory body force is evaluated for a range of fluid properties.

1. Introduction

Multiphase flow of viscous fluids through porous media is a problem of fundamental importance in the petrochemical industry, with specific application to oil recovery. To model multiphase flow, many studies have considered the flow of droplets through capillary tubes with both straight and constricted geometries. The efficacy of using these models for flow through porous media, as well as studies which detail their flow behaviour have been reviewed by Olbricht (1996). Recently, we have become interested in the unsteady motion of droplets that arises for oscillatory forcing. Our motivation is the enhanced efficiency of secondary oil recovery operations that may occur when strong acoustic stimulation is added to a reservoir.

Secondary oil recovery is a process in which water is injected into a reservoir through a network of supply wells in an attempt to force the oil out of a central production well. Both field tests and laboratory experiments have demonstrated that strong acoustic stimulation delivered to an oil reservoir may enhance the efficiency of secondary oil recovery by increasing the production of oil and reducing the volume fraction of water in the product stream (Beresnev & Johnson 1994). While the results of these tests are intriguing, there has been no rigorous physical explanation for the enhanced oil recovery associated with acoustic stimulation.

To examine the fundamental physical processes relevant to acoustic stimulation of porous media, we assume that the porous medium is a porous elastic solid into which a travelling acoustic wave is introduced by an external stimulus. The propagation of acoustic waves in fluid-saturated porous media has been the subject of much study in the literature dating from the early work of Biot (1956*a*, *b*). Chapman & Higdon (1992, 1994) present a review of recent work covering the theory for the dynamics of both the fluid and the solid phases. For acoustic wavelengths which are large compared to the characteristic pore size, the coupling of the fluid dynamics and the solid mechanics is significantly simplified. The long distance wave propagation occurs primarily through the elastic deformation in the solid phase, while the fluid motion acts as a relatively short-range damping force. The acoustic wave induces a large-scale motion of the solid phase which provides an accelerating reference frame for the microscopic fluid motion. For the fluid motion on the microscopic scale, the governing equations reduce to those for an incompressible fluid flowing through a rigid porous medium with an oscillatory body force accounting for the action of the accelerating reference frame. With this background, we infer that the effects of acoustic stimulation on porous media may be studied by considering pore-scale fluid flows subject to the simultaneous action of a mean pressure gradient and an oscillatory body force.

In a recent study, we described some of the fundamental physical processes relevant to this phenomenon by focusing on regions of the porous medium where oil and water flow independently (Graham 1997). We conducted an investigation of the effects of acoustic stimulation on single-phase flow. We showed that the inertial forces resulting from acoustic stimulation may decrease the water flow rate and leave the flow of oil unimpeded. The goal of the present paper is to extend our previous single-phase flow investigation to determine how interfacial effects influence acoustic stimulation of multiphase flows.

Early theoretical work on the flow of drops in capillary tubes was conducted by Bretherton (1961). In this work, Bretherton used lubrication analysis to determine the scaling for the pressure drop ΔP across the droplet with capillary number Ca and showed that

$$\Delta P \sim Ca^{2/3}. \tag{1.1}$$

This scaling was later shown to be valid for droplets with viscosity ratio up to $O(Ca^{-1/3})$ (Park & Homsy 1984). On the experimental side, Ho & Leal (1975) conducted a series of experiments to study droplet motion in capillaries over a wide range of conditions. These authors showed that the extra pressure drop due to the droplet (ΔP^+) can be positive or negative, depending on a complex interplay between viscosity ratio λ and surface tension. Drops with $\lambda > 1$ have a positive ΔP^+, but droplets with $\lambda < 1$ can have either a positive or a negative ΔP^+. For the $\lambda < 1$ case, factors that lead to a positive ΔP^+ are a decrease in either the capillary number or in the drop size.

To complement the above experimental and theoretical studies, a computational study of droplet flow was conducted by Martinez & Udell (1990). These authors used a boundary integral formulation to analyse the Stokes flow behaviour for a wide variety of drop sizes, viscosity ratios and capillary numbers. Furthermore, they verified many of the findings of Ho & Leal, and determined that the drop shape and speed become size independent once the drop radius exceeds a critical value.

In addition to the work on pressure-driven motion of droplets, several researchers have examined the motion of droplets due to the action of buoyancy forces. Pozrikidis (1992) presents numerical computations for the buoyancy-driven flow of a train of viscous droplets under Stokes flow conditions. Detailed droplet shapes are presented, along with a discussion of the effects of Bond number on the terminal velocity of the droplets. The combined effects of pressure gradients and buoyancy forces were studied by Borhan & Pallinti (1998). The buoyancy force was found to increase the velocity of the droplet relative to the bulk fluid and to modify the drop shapes slightly. While the above studies examined low Reynolds number flow, a recent paper by Bozzi *et al.* (1997) presents results for moderate Reynolds numbers. These authors focused on small drops and documented the changes in drag coefficient due to inertial effects.

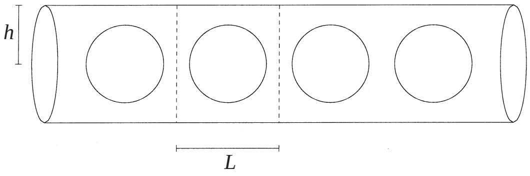

FIGURE 1. Schematic of capillary tube.

While extensive work has been devoted to steady-state drop flow through capillary tubes and other geometries, unsteady flow has received less attention. One exception is the work of Coulliette & Pozrikidis (1998), who examined the non-axisymmetric motion of drops displaced from the centreline of the tube. There has been a large body of research devoted to unsteady droplet behaviour; however, this work has focused on droplet motion in an unbounded fluid. Examples include the early theoretical analyses of Miller & Scriven (1968) and Tsamopolous & Brown (1983) and the more recent computational work of Basaran (1992).

In the current effort, we study oscillatory droplet motion in confined domains representative of porous media. Here we consider flow in straight capillary tubes; in Part 2 (Graham & Higdon 2000) we consider flow in constricted tubes. We analyse the effects of acoustic stimulation on the droplet motion, calculating the flow rates of both the droplet and suspending phase over a wide range of conditions. Our goal is to determine how the application of acoustic stimulation enhances the mean flow rate compared to a base flow driven solely by a mean pressure gradient.

2. Problem formulation

2.1. *Governing equations*

We consider the flow of a periodic suspension of fluid droplets (period L) in a straight capillary tube (radius h) as show in figure 1. The size of the drops is characterized by the volume V or the equivalent radius a, where $V = \frac{4}{3}\pi a^3$. The governing equations for the flow of a constant-property Newtonian fluid are the Navier–Stokes equations and the continuity equation

$$\rho\left(\frac{\partial \boldsymbol{u}}{\partial t} + \boldsymbol{u}\cdot\nabla\boldsymbol{u}\right) = \nabla\cdot\boldsymbol{\sigma} + \boldsymbol{b}, \tag{2.1}$$

$$\nabla\cdot\boldsymbol{u} = 0, \tag{2.2}$$

where $\boldsymbol{\sigma}$ is the stress tensor

$$\sigma_{ij} = -P\delta_{ij} + \mu\left(\frac{\partial u_i}{\partial x_j} + \frac{\partial u_j}{\partial x_i}\right) \tag{2.3}$$

and $\boldsymbol{b}$ is a body force. In this paper, we consider flow driven by the combined action of a mean pressure gradient and an oscillatory body force. The mean pressure gradient can be absorbed into a constant body force G_o, and the total body force becomes

$$b_z = G_o + G_{rms}g(t) \tag{2.4}$$

in which $g(t)$ is a periodic function with unit root-mean-square amplitude and period τ. For an acoustic wave, the equivalent oscillatory body force is proportional to the fluid density, and therefore the force on the droplet may be different from the force on the suspending fluid.

We assume that the continuous phase has viscosity μ and density ρ, while the droplet has viscosity $\lambda\mu$ and density $\rho_D\rho$. Because of the difference in fluid properties, a separate system of governing equations is written for each phase. These two systems are coupled due to the boundary conditions on the surface of the drop. We impose the traction boundary condition representing the jump in stress at the interface

$$(\boldsymbol{\sigma}\cdot\boldsymbol{n})_{12} = (\gamma\nabla\cdot\boldsymbol{n})\boldsymbol{n}, \tag{2.5}$$

where γ is the surface tension and $\boldsymbol{n}$ is the normal vector. Also, we employ the kinematic condition

$$\boldsymbol{u}\cdot\boldsymbol{n} = \frac{\mathrm{d}\boldsymbol{x}}{\mathrm{d}t}\cdot\boldsymbol{n} \tag{2.6}$$

to determine the position of the interface.

At the centre of the tube we impose the symmetry conditions,

$$u_r = 0, \quad \boldsymbol{e}_z\cdot(\boldsymbol{\sigma}\cdot\boldsymbol{n}) = 0, \tag{2.7}$$

where $\boldsymbol{e}_z$ is a unit vector in the z-direction. On the surface of the tube walls the no-slip condition is imposed,

$$\boldsymbol{u} = \boldsymbol{0}. \tag{2.8}$$

At the inlet and the outlet of the tube we impose periodic boundary conditions,

$$\boldsymbol{u}(r,z) = \boldsymbol{u}(r,z+L) \tag{2.9}$$

and

$$P(r,z) = P(r,z+L). \tag{2.10}$$

Here, the pressure is periodic because the mean gradient has been absorbed into the body force.

2.2. *Non-dimensional parameters*

Having defined the physical problem to be solved, we turn our attention to the parameters which characterize the flow. Both the steady and oscillatory components of the body force are non-dimensionalized with respect to the tube radius and surface tension, hence

$$F_o = G_o h^2/\gamma, \tag{2.11}$$

$$F_{rms} = G_{rms} h^2/\gamma. \tag{2.12}$$

The frequency of forcing is characterized by the period τ and a non-dimensional frequency may be defined by scaling τ with the viscous response time of the droplet:

$$f = \frac{a\mu}{\tau\gamma}. \tag{2.13}$$

The parameters above serve to specify the applied driving forces, while the remaining parameters characterize the fluid properties. The viscosity ratio λ and the density ratio ρ_D have been defined previously. The drop-phase volume fraction is defined by

$$\phi = \frac{V}{L\pi h^2}. \tag{2.14}$$

The final parameter is the material property number based on the fluid properties ρ, μ, γ and the capillary size h. This parameter is equal to the ratio of the Reynolds number to the capillary number

$$\frac{Re}{Ca} = \frac{\rho h \gamma}{\mu^2}. \tag{2.15}$$

We specify the parameters given above and solve for the velocity field and the droplet shape. Several quantities are useful to characterize the magnitude of the flow rate in the capillary. For steady flow, we define the bulk fluid velocity as

$$U_{ss} = \frac{1}{\pi h^2} \int_0^h \boldsymbol{u} \cdot \boldsymbol{n} \, 2\pi r \, \mathrm{d}r, \tag{2.16}$$

and non-dimensionalize by defining a capillary number

$$Ca = \frac{U_{ss}\mu}{\gamma}. \tag{2.17}$$

An alternative measure of the bulk flow rate is the dimensionless permeability

$$\kappa = \frac{\mu U_{ss}}{G_o h^2}. \tag{2.18}$$

The most useful parameter characterizing the flow resistance of the droplets is the extra pressure drop ΔP^+

$$\Delta P^+ = \Delta P^{tot} - \Delta P^{para}. \tag{2.19}$$

Here, the total pressure drop ΔP^{tot} is given in terms of the the mean gradient by $\Delta P^{tot} = G_\circ L$, and ΔP^{para} is the equivalent pressure drop for a single-phase flow at the same bulk flow rate, i.e.

$$\Delta P^{para} = \frac{8\mu U_{ss} L}{h^2}. \tag{2.20}$$

For unsteady flow, the bulk fluid velocity varies with time according to

$$U(t) = \frac{1}{\pi h^2} \int_0^h \boldsymbol{u}(t) \cdot \boldsymbol{n} \, 2\pi r \, \mathrm{d}r, \tag{2.21}$$

and the meaningful flow parameter is the long time average defined by

$$U_{bulk} = \lim_{t_2 \to \infty} \frac{1}{t_2 - t_1} \int_{t_1}^{t_2} U(t) \, \mathrm{d}t. \tag{2.22}$$

For the oscillatory forcing studied in this paper, the quantity which best characterizes the enhanced transport rates is the ratio of the bulk velocity with oscillatory forcing to the bulk velocity in the absence of oscillatory forcing. We define the velocity enhancement factor

$$U_E = \frac{U_{bulk}}{U_{ss}}, \tag{2.23}$$

where the subscript E indicates that this quantity reflects the *enhancement* in flow rate. To quantify the speed of the droplet we employ the ratio of drop speed to bulk velocity U_{drop}/U_{bulk}, where U_{drop} is defined as the average speed of the drop centroid.

To end this section, it may be helpful to note typical values of the system parameters for acoustic stimulation in oil reservoirs. For a typical reservoir, a characteristic velocity is 3.5×10^{-4} cm s^{-1} (1 foot/day). With a characteristic permeability of 10^{-8} cm^2 and viscosity of 0.1 g cm^{-1} s^{-1}, this requires a pressure gradient of 3.5×10^3 g cm^{-2} s^{-2}. For a surface tension of 40 dyn cm^{-1} (appropriate for oil–water systems), the steady-state capillary number in the reservoir would be of order 10^{-6}. For acoustic stimulation, the

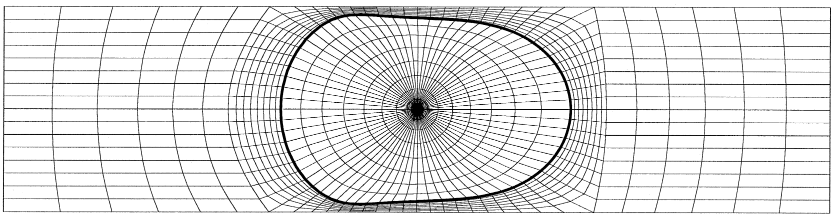

FIGURE 2. Typical finite element mesh.

amplitude of the oscillatory force is given by $G_o = 4\pi^2 \rho d/\tau^2$, where d is the displacement of the acoustic wave. With displacements of 20 μm at a frequency of 500 Hz, the oscillatory force is $2 \times 10^4\,\mathrm{g\,cm^{-2}\,s^{-2}}$. Therefore, conditions of special interest for acoustic stimulation of porous media are low-*Ca* flows where the oscillatory force is larger than the mean pressure gradient.

3. Numerical methods

The governing equations are solved via the Galerkin finite element method. This method requires the development of a computational grid, the formation of the residual equations and the solution of these equations.

3.1. *Grid generation*

The development of a computational grid consists of mapping the physical domain (r, z) to a simplified domain (ξ, η). The development of this mapping is especially challenging for free-surface problems because the position of the interface is unknown *a priori*. The mesh generation scheme must efficiently track the interface and maintain accuracy throughout the entire domain. In our case, this is achieved using a technique known as elliptic grid generation (Thompson, Warsi & Mastin 1985). In this formulation, elements in the physical domain are mapped to square elements via the solution to a system of elliptic partial differential equations,

$$\nabla \cdot D_\xi \nabla \xi = 0, \tag{3.1}$$

$$\nabla \cdot D_\eta \nabla \eta = 0, \tag{3.2}$$

where D_ξ and D_η are adjustable parameters that allow for local grid refinement on the interior of the physical domain.

The boundary of the computational domain and the drop interface is defined by imposing Dirichlet boundary conditions on the above equations. In our formulation, we arbitrarily specify curves of constant η to represent the boundary of the domain and the surface of the drop, and let ξ measure the distance along each curve. At the surface of the drop, the kinematic condition is imposed on the η equation (3.2). For the ξ equation (3.1), we impose a Dirichlet condition which maintains an efficient point distribution based on a weighted combination of the arc length and the angle spanned by adjacent elements. For points sufficiently far from the drop, grid generation is much less challenging, and we employ simple algebraic formulas to determine the grid point locations (Thompson *et al.* 1985). A typical mesh generated with the hybrid elliptic/algebraic grid algorithm is shown in figure 2.

3.2. *Galerkin finite element method*

The Navier–Stokes (equation (2.1)), continuity (equation (2.2)) and grid generation equations ((3.1) and (3.2)) are solved simultaneously with the Galerkin finite element method (Gunzberger 1989). In our implementation, we approximate the velocity, the pressure and the position vectors of the grid points as

$$\boldsymbol{u} = \sum_{i=1}^{N} u_i \psi_i, \tag{3.3}$$

$$P = \sum_{i=1}^{M} P_i \phi_i, \tag{3.4}$$

$$\boldsymbol{x} = \sum_{i=1}^{P} x_i \theta_i, \tag{3.5}$$

where ψ_i, ϕ_i and θ_i are the basis functions u_i, P_i and x_i are the nodal values, and N, M, and P are the number of equations, for velocity, pressure and grid point locations, respectively. We use nine-node quadrilateral elements with biquadratic basis functions to approximate velocities. We employ three linear basis functions for pressure, which are discontinuous at element boundaries. This element pair is stable and satisfies conservation of mass on each element (Gunzberger 1989).

The governing equations are solved simultaneously with the grid generation equations. To reduce the computational burden of solving this combined system, we employ subparametric mapping. For elements that do not border the droplet, we use bilinear basis functions for the geometry variables, and the solution to equations (3.1) and (3.2) yields the position of the nodes on the corner of each element. The positions of the interior points are determined using simple interpolation formulas given by Christodoulou & Scriven (1992). We modify the elements which border the drop so that three nodes represent the edge of the drop (Hughes 1987).

Grid generation is facilitated by solving the problem in a reference frame that moves with the drop. The speed of the reference frame u_{ref} is unknown and is determined by adding a constraint equation that requires the drop to remain at the origin of the computational domain, or

$$\int_V z \, \mathrm{d}V = \int_{S_d} z \pi r^2 \frac{\mathrm{d}z}{\mathrm{d}s} \, \mathrm{d}s = 0. \tag{3.6}$$

For unsteady problems, an adjustment of the speed of the reference frame leads to an accelerating reference frame, which is equivalent to a body force acting in the negative z-direction with magnitude $\rho \partial u_{ref}/\partial t$. This quantity is subtracted from the prescribed body force $b_z(t)$ to yield the force used in our implementation $b'_z(t)$:

$$b'_z(t) = b_z(t) - \rho \frac{\partial u_{ref}}{\partial t}. \tag{3.7}$$

Since the grid point locations are constantly updated in time, we must transform the time derivatives in equation (2.1) at fixed locations in space to fixed isoparametric locations. The following transformation is employed:

$$\frac{\partial \boldsymbol{u}}{\partial t} = \dot{\boldsymbol{u}} - \dot{\boldsymbol{x}} \cdot \nabla \boldsymbol{u}, \tag{3.8}$$

where $\dot{\boldsymbol{x}}$ represents the mesh velocity (Christodoulou & Scriven 1992).

Following Galerkin's method, we form the weighted residuals of equations (2.1), (2.2), (3.1), (3.2) and (3.6), integrate over the entire domain, and apply the divergence theorem to yield the final form

$$\boldsymbol{R}_i^M = \int_V \psi^i \boldsymbol{e}_k \cdot \left[\rho(\dot{\boldsymbol{u}} + (\boldsymbol{u} - \dot{\boldsymbol{x}}) \cdot \nabla \boldsymbol{u}) - \boldsymbol{b}'\right] + \boldsymbol{\sigma} : \nabla(\psi^i \boldsymbol{e}_k)\, \mathrm{d}V - \int_S \psi^i \boldsymbol{e}_k \cdot (\boldsymbol{\sigma} \cdot \boldsymbol{n})\, \mathrm{d}S = 0, \quad (3.9)$$

$$\boldsymbol{R}_j^C = \int_V \phi^j \nabla \cdot \boldsymbol{u}\, \mathrm{d}V = 0, \quad (3.10)$$

$$\boldsymbol{R}_l^{G,\xi} = \int_V \nabla\theta^l \cdot (D_\xi \nabla \xi)\, \mathrm{d}V - \int_S \boldsymbol{n} \cdot (D_\xi \nabla \xi)\theta^l\, \mathrm{d}S = 0, \quad (3.11)$$

$$\boldsymbol{R}_l^{G,\eta} = \int_V \nabla\theta^l \cdot (D_\eta \nabla \eta)\, \mathrm{d}V - \int_S \boldsymbol{n} \cdot (D_\eta \nabla \eta)\theta^l\, \mathrm{d}S = 0 \quad (3.12)$$

and

$$R^P = \int_{S_d} z\pi r^2 \frac{\mathrm{d}z}{\mathrm{d}s}\, \mathrm{d}s = 0. \quad (3.13)$$

The superscripts M, C, G and P refer to the momentum, continuity, grid, and position constraint equations respectively and $\boldsymbol{e}_k$ is a unit vector in either the r- or z-direction. We solve this system simultaneously to calculate the velocities and grid point location of each node. The kinematic condition is imposed via Dirichlet boundary conditions on the grid equations. For steady-state problems, we replace the kinematic condition at one node on the surface of the drop with a constraint on the volume of the drop.

3.3. *Steady-state solution*

For convenience, we rewrite the above system of nonlinear algebraic equations as

$$R_i(x_j) = 0, \quad (3.14)$$

where R_i is a vector of residuals corresponding to the momentum, continuity and grid equations and x_j is a vector of unknowns corresponding to the nodal values of velocity, pressure and grid point locations. This system is solved iteratively with Newton's method (Goodwin & Schowalter 1996)

$$\left(\frac{\partial R_i}{\partial x_j}\right)^k \Delta x_j^{k+1} = -R_i^k, \quad (3.15)$$

where the superscript k is the iteration number, Δx_j is the change in nodal values and $\partial R_i/\partial x_j$ is the analytically evaluated Jacobian matrix. All integrals in this equation are evaluated with three-point Gauss–Legendre quadrature (Carnahan, Luther & Wilkes 1969), and the equations are solved with UMFPACK, a code that implements a frontal method (Davis 1995).

As with other iterative techniques, Newton's method requires an initial guess for the velocity field. For steady-state problems, one efficient procedure is to obtain a velocity field at a low forcing level, using $\boldsymbol{u} = \boldsymbol{0}$ as the initial guess, and to apply continuation in F_o. For our initial profile we employ strong surface tension so that the shape of the droplet can be closely approximated by a sphere. In addition to continuation in F_o, we have found that continuation in a/h is an effective means to find solutions for drops that have a radius larger than the radius of the tube. With these continuation methods, one may easily obtain solutions for desired values of either the steady forcing level F_o or the capillary number Ca.

Mesh	Elements	Unknowns	Ca	$\frac{\Delta P^{+}h}{\gamma}$
M1	68	988	3.1377×10^{-4}	0.043918
M2	208	2922	3.5615×10^{-4}	0.041206
M3	672	9034	3.5552×10^{-4}	0.041246
M4	1040	13851	3.5476×10^{-4}	0.041295

TABLE 1. Convergence data for F_o=0.008, $\lambda = 1$, $\rho_D = 1$, $a/h = 1.1$, $\phi = 0.2218$, $Re/Ca = 31.25$. For mesh M3, approximately 75 s per iteration were required.

Mesh	Elements	Unknowns	Ca	$\frac{\Delta P^{+}h}{\gamma}$
M1	68	988	0.0998652	0.375543
M2	208	2922	0.0998951	0.373626
M3	672	9034	0.10000466	0.366614
M4	1040	13851	0.10001167	0.366166

TABLE 2. Convergence data for F_o=0.845864, $\lambda = 1$, $\rho_D = 1$, $a/h = 1.1$, $\phi = 0.2218$, $Re/Ca = 0$.

To test the accuracy of the above algorithm, we conducted convergence tests as shown in tables 1 and 2 for two distinct forcing levels. For both forcing levels, Ca and ΔP^{+} each change by less than 0.25% between meshes M3 and M4. Therefore mesh M3 (figure 2) provides sufficient accuracy and will be used for the remainder of this paper. Furthermore, for higher forcing levels, we note that ΔP^{+} is more sensitive to grid refinement than Ca, indicating that convergence in Ca is not sufficient to ensure an accurate calculation of ΔP^{+}. As an independent check of the results presented in table 2, we performed the same calculation using a spectral boundary integral technique (Muldowney & Higdon 1994). Excellent agreement was obtained, with the Ca accurate to 0.01% and ΔP^{+} accurate to 0.25%. Comparison with the computations of Martinez & Udell (1992) also shows good agreement with the predicted droplet length and wall film thickness to within 2%. Those authors showed that their results were consistent with the experiments of Olbricht & Kung (1992) with variations of 5% and 8% in the droplet length and film thickness respectively. Additional comparisons with relevant results from Bozzi *et al.* (1997) verified that finite Re effects are captured correctly in the present computations.

3.4. *Predictor-corrector scheme for unsteady flows*

For unsteady problems, the introduction of the finite element approximations for velocity and pressure leads to a system of nonlinear algebraic differential equations. These equations must be integrated in time to obtain the velocity field and droplet shape at every time step. We perform the integration with an explicit Adams–Bashforth prediction, followed by an implicit trapezoidal rule correction, as described by Gresho, Lee & Sani (1980). Following Gresho, we have implemented an adaptive time-step scheme with a relative error tolerance of 0.001 between the predicted solution and the corrected solution.

To begin the unsteady calculations, we first calculate the steady-state velocity profile corresponding to a given steady forcing level. The overall time required for the unsteady simulations can be reduced by selecting the initial profile to have a deformation similar to the average value of the deformation expected. We perform

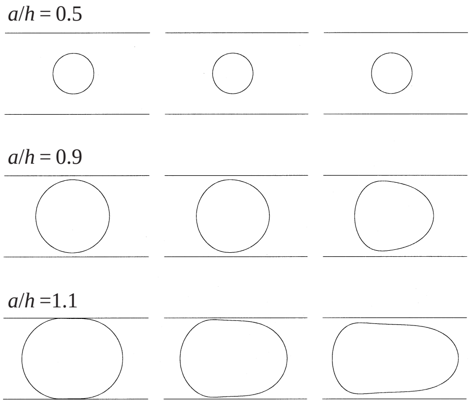

FIGURE 3. Steady-state drop shapes for three different drop sizes at three different capillary numbers. For each drop size, $Ca = 5 \times 10^{-4}$, $Ca = 0.01$ and $Ca = 0.05$ are shown. Additional parameters are $\lambda = 1$, $\rho_D = 1$, $\phi = 0.2218$, $Re/Ca = 31.25$.

five time steps with a backward Euler method at a fixed time step, before switching to the trapezoidal rule scheme with automatic time step selection. Using a backward-difference method for the initial time steps avoids unwanted oscillations that can potentially occur in the trapezoidal rule as a result of certain initial conditions (Kheshgi & Scriven 1984). The above algorithm was tested by comparing results to the analytical solution for oscillatory flow in a straight capillary tube.

4. Results: steady state

The steady flow behaviour of a droplet in a capillary tube is a function of the drop size a/h, capillary number Ca, viscosity ratio λ, density ratio ρ_D, material property number Re/Ca, and the droplet volume fraction ϕ. In this section we focus on how the computed drop shapes and the pressure drop vary with drop size and capillary number. In figure 3, we begin by presenting steady-state drop shapes for three different drop sizes at three different capillary numbers. The smallest drops ($a/h = 0.5$) show negligible deformation for the capillary numbers shown. As we move to larger drop sizes ($a/h = 0.9, 1.1$), figures 3(*b*) and 3(*c*) show a progressive increase in drop deformation with increasing capillary number. For drop sizes larger than those shown here, additional computations show drop shapes consistent with those for $a/h = 1.1$ with more elongation in the flow direction. These results are consistent with the observations of Martinez & Udell (1990).

Next, we examine the pressure drop in the tube as a function of capillary number and drop size. An important contribution to the total pressure drop is the extra pressure change due to the droplet ΔP^+. This quantity is closely related to the capillary pressure encountered in reservoir modelling which characterizes the extra flow resistance due to interfacial forces. In the present study, the pressure change ΔP^+, defined by equation (2.19), measures the total pressure effect of the droplet including viscous and interfacial forces. It should be noted however that the interfacial forces are dominant for capillary numbers of interest, and hence this quantity accurately reflects the capillary pressure. In figure 4 we plot the ratio of ΔP^+ to the total pressure drop ΔP^{tot} as a function of Ca. This figure shows that the magnitude of ΔP^+ decreases relative to ΔP^{tot} as the capillary number increases, consistent with expectations for decreasing surface tension. The pressure drop ΔP^+ shows significant variation for the

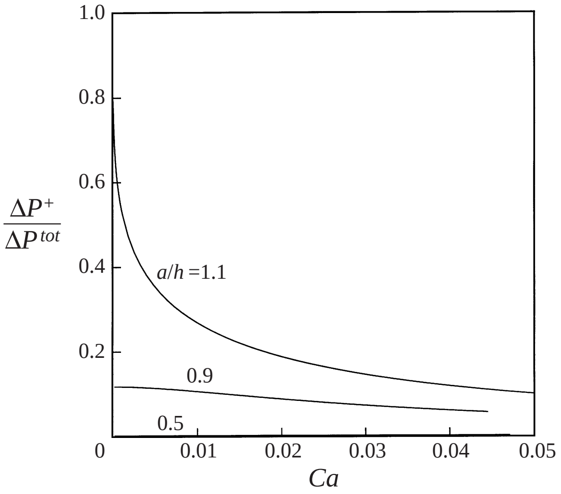

FIGURE 4. Extra pressure drop as a function of capillary number for $\lambda = 1$, $\rho_D = 1$, $\phi = 0.2218$ and $Re/Ca = 31.25$.

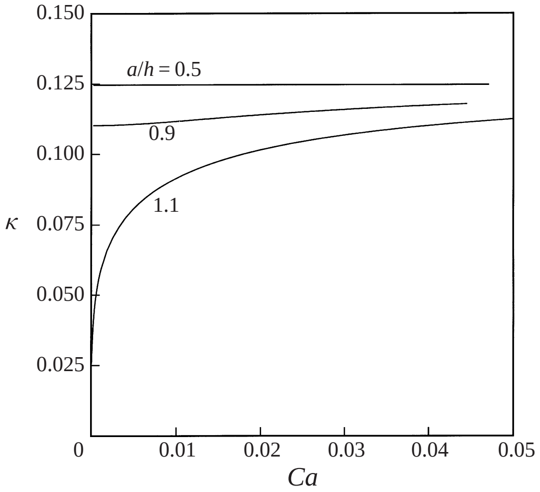

FIGURE 5. Permeability κ as a function of capillary number Ca for $\lambda = 1$, $\rho_D = 1$, $\phi = 0.2218$ and $Re/Ca = 31.25$.

large drops $a/h = 1.1$, but much smaller variation for the smaller drop sizes. (Note that the curve for $a/h = 0.5$ is nearly coincident with the horizontal axis.) For large drops at low Ca, a thin lubrication layer forms between the droplet and the tube wall, and the high shear stress in this layer increases ΔP^+. As Ca increases, the drop deforms and admits a larger volume of fluid into the lubrication layer. As a result, the shear stresses are reduced and ΔP^+ decreases relative to ΔP^{tot}. The decrease in ΔP^+ for drops with $a/h = 1.1$ leads to a significant increase in the overall permeability κ as Ca increases (figure 5). For smaller drop sizes, the permeability is only a weak function of Ca.

The thin lubrication layers which develop for large droplets at small capillary numbers greatly increase the difficulty of the numerical computations. The gap between the tube wall and the drop interface becomes much thinner, and the required

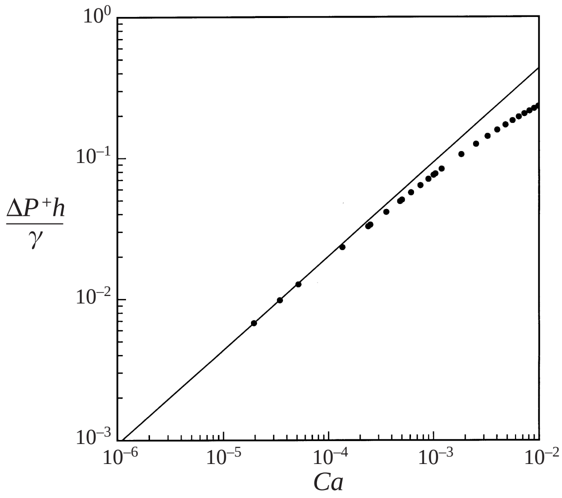

FIGURE 6. Extra pressure drop $\Delta P^+ h/\gamma$ as a function of capillary number Ca for $\lambda = 1$, $\rho_D = 1$, $\phi = 0.2218$ and $Re/Ca = 31.25$. The circles represent calculated data points and the solid line is asymptotic result with slope of 2/3.

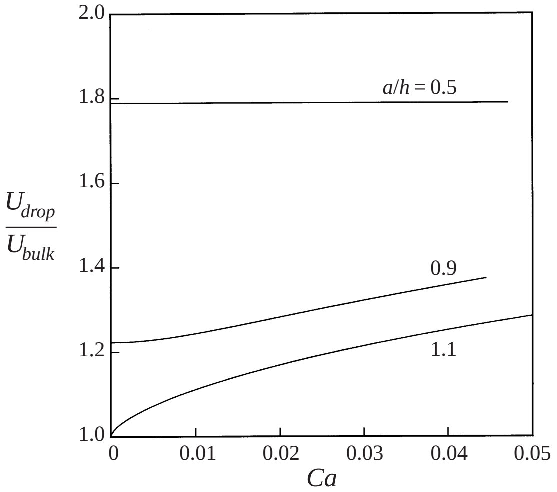

FIGURE 7. Relative drop velocity as a function of capillary number for drops with $\lambda = 1$, $\rho_D = 1$, $\phi = 0.2218$, $Re/Ca = 31.25$.

spatial resolution increases dramatically. As an alternative to numerical computations at very low capillary numbers, we will utilize the asymptotic scaling results for ΔP^+ as $Ca \rightarrow 0$. Figure 6 presents a log-log plot of ΔP^+ versus Ca, showing good convergence to the asymptotic prediction $\Delta P^+ \sim Ca^{2/3}$ for viscous drops obtained by Park & Homsy (1984). The numerical data in this figure provide the coefficient for the $Ca^{2/3}$ dependence and allow us to make quantitative predictions in the asymptotic regime.

Turning our attention from the bulk flow rate to the drop speed, we plot the ratio of the drop speed to bulk flow rate as a function of capillary number in figure 7. Small drops travel at almost twice the bulk velocity owing to the nearly parabolic velocity profile in the tube. By contrast, larger drops travel at nearly the same speed as the bulk fluid for low Ca, but show a marked velocity increase relative to the bulk as Ca increases. This increase in speed is due to the increased deformation at higher Ca, which allows the droplet to remain closer to the centre of the tube where the local fluid velocities are greater. Note that the relative drop velocity is a direct measure of the relative permeability of the two phases. (Recall that the permeability is proportional to the velocity.) Thus an increase in (oil) droplet velocity represents an increase in the relative permeability for the dispersed (oil) phase.

In summary, our steady-state results have shown that both the permeability κ and the relative droplet velocity U_{drop}/U_{bulk} are strong functions of Ca, and hence have strong dependence on the applied forcing level. As the forcing level increases, droplet deformation increases, which causes ΔP^+ to decrease and the permeability to increase. The increased droplet deformation also leads to an increase in the relative droplet velocity.

5. Quasi-steady analysis

Having characterized the flow of droplets in capillary tubes under steady flow conditions, we turn our attention to the droplet motion under oscillatory forcing conditions. In the presence of oscillatory forcing, both the droplet velocity and the bulk fluid velocity are functions of time. For very small oscillatory frequencies, the driving force changes sufficiently slowly that the droplet shape and the fluid velocity profile are well approximated by their steady-state values evaluated at each instantaneous forcing level. Under these conditions, the unsteady velocities can be obtained from steady-state data as

$$U(t) = U_o(F)\big|_{F=F(t)}, \tag{5.1}$$

in which $U(t)$ and U_o represent either the bulk fluid velocity or the droplet velocity and $U_o(F)$ is the steady-state velocity at a given forcing level F. The primary focus of this section will be to use the quasi-steady approximation to calculate the mean flow rate under a wide range of conditions. The mean flow is computed as

$$\overline{U} = \frac{1}{\tau}\int_0^{\tau} U_o(F(t))\,\mathrm{d}t, \tag{5.2}$$

where the range of integration is over one period of oscillation.

This quasi-steady approximation is valid when the time scale of the applied forcing τ is much larger than the other time scales in the problem. When a fluid droplet is subject to deformation in a flow, surface tension acts to return the drop to an undeformed state. The surface tension is opposed by the viscous resistance of the fluid and by its inertia. Owing to these factors, there are two time scales associated with the response of a droplet to changes in forcing level. These are the viscous response time $t_v = \mu a/\gamma$ and the inertial response time $t_i = \sqrt{\rho a^3/\gamma}$. The ratio of these two time scales is simply $t_i/t_v = \sqrt{Re/Ca}$, so that we may interpret the material property number Re/Ca as a measure of the inertial to viscous response time of the droplet. For quasi-steady analysis, we require that $t_v/\tau \ll 1$ and $t_i/\tau \ll 1$. In addition to the response time of the droplet, there is a characteristic time scale for the suspending fluid, represented by the viscous diffusion time scale $t_\mu = \rho a^2/\mu$. The ratio t_μ/τ must also be small.

In terms of dimensionless parameters, the three conditions $t_v/\tau \ll 1$, $t_i/\tau \ll 1$ and

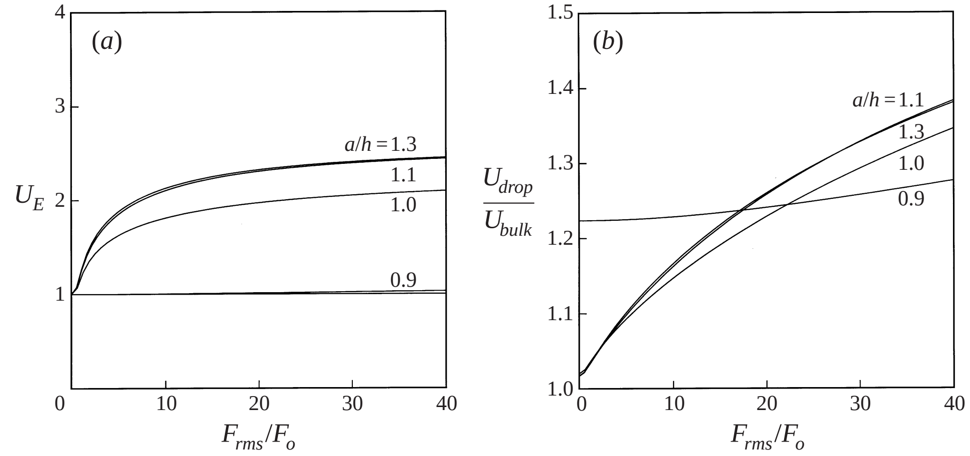

FIGURE 8. Flow rate as a function of oscillatory forcing for different drop sizes and $Ca = 5 \times 10^{-4}$, $\lambda = 1$, $\rho_D = 1$, $\phi = 0.2218$, $Re/Ca = 31.25$ with sinusoidal forcing: (*a*) bulk fluid, (*b*) relative drop velocity.

$t_\mu/\tau \ll 1$ are given by the respective conditions

$$f \ll 1, \quad f\sqrt{Re/Ca} \ll 1, \quad f(Re/Ca) \ll 1. \tag{5.3}$$

Obviously, when the first and third conditions are satisfied, the second will be satisfied automatically. While the quasi-steady approximation is strictly valid only in these asymptotic limits, we shall show that the trends observed here are qualitatively similar to those for the full unsteady simulations over a wide range of frequencies.

In the following subsections, we consider sinusoidal forcing functions ($g(t) = \sin(2\pi t/\tau)/\sqrt{2}$ in equation (2.4)) and examine the effects of oscillatory forcing on the mean flow rate for different parameters over a wide range of geometric and fluid properties. We then examine a different temporal forcing function in an effort to optimize the changes in mean flow rate that arise with oscillatory forcing.

5.1. *Drop size effects*

We begin our investigation by studying droplets of different sizes a/h relative to the radius of the capillary tube. Recall that we consider the motion of a droplet subject to a steady force F_o and a sinusoidal force with root-mean-square value F_{rms}. In figure 8, we present the enhancement in flow rate as a function of oscillatory forcing for different drop sizes. For the quasi-steady regime, recall that the flow behaviour of the oscillatory system may be predicted from the data for steady-state solutions. The relevant data we require are those for permeability from figure 5. In that figure, we saw that the permeability for small droplets $a/h \leqslant 0.9$ is essentially constant, independent of Ca (or forcing level). The bulk velocity at any instant in the oscillatory flow is equal to the product of the instantaneous forcing level and the permeability for that forcing level. When the permeability is constant, the effect of the oscillatory pressure averages to zero and there is no enhancement. This is reflected in the curve for small droplets ($a/h \leqslant 0.9$) in figure 8. For larger droplets, figure 5 showed a dramatic increase in permeability with increasing Ca or (forcing level F_o). When the oscillatory pressure is positive, acting with the mean pressure gradient, the total forcing level is higher, leading to greater permeability and a nonlinear increase in velocity. When the oscillatory force is negative, the overall force is lower leading to lower permeability

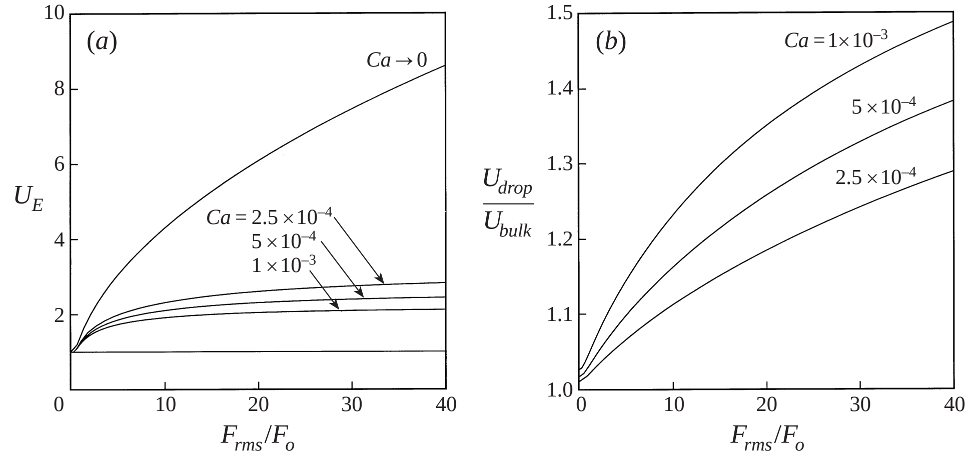

FIGURE 9. Flow rate as a function of oscillatory forcing for different capillary numbers and $a/h = 1.1$, $\lambda = 1$, $\rho_D = 1$, $\phi = 0.2218$, $Re/Ca = 31.25$ with sinusoidal forcing: (*a*) bulk fluid, (*b*) relative drop velocity.

and a nonlinear reduction in the velocity. The net result of the nonlinearity is a positive contribution to the time-average velocity over the period of the oscillatory force cycle. The effect of this permeability-induced nonlinearity is seen in the curves for large droplets $a/h \geqslant 1.1$ in figure 8 which show a strong enhancement in the overall flow rate. Given the similarity between the results for drops with $a/h = 1.3$ and $a/h = 1.1$, we infer that $a/h = 1.1$ accurately reflects the asymptotic behaviour for long drops. Therefore, for subsequent results, we will focus on drops with $a/h = 1.1$.

5.2. *Capillary number effects*

Next, we consider the effect of surface tension on the enhancement of the flow rate. In particular, we consider droplets with different capillary numbers, where the capillary number is based on the bulk flow rate in the absence of oscillatory forcing. In figure 9(*a*), we show the effect of oscillatory forcing on the bulk fluid flow rate for three different steady-state capillary numbers and for the low-capillary-number asymptotic limit. In the small-Ca limit, the total pressure drop is essentially equal to ΔP^+, and therefore we assume that $F \sim Ca^{2/3}$ throughout the forcing cycles for the $Ca \to 0$ curve. As the steady capillary number in the base flow increases, the enhancement in mean flow rate achieved by the acoustic forcing decreases. For these higher capillary numbers, ΔP^+ decreases relative to the total pressure drop, and therefore the reduction in ΔP^+ due to the oscillatory forcing has less effect on the overall flow rate.

Turning our attention from the bulk fluid flow rate to the droplet velocity, we plot the ratio of drop velocity to bulk velocity as a function of oscillatory forcing in figure 9(*b*). Here, we observe that the relative drop speed increases with the level of oscillatory forcing, but that the speed increase is less pronounced for lower capillary numbers. For these low capillary numbers, the drop deformation is smaller, and therefore the velocity of these large droplets remains closer to the bulk velocity.

5.3. *Reynolds number effects*

The Reynolds numbers for the computations presented to this point have been in the range where inertial effects are negligible ($Re_o = 0.0156$). While this is the most appropriate range for oil recovery processes, we examine results for higher

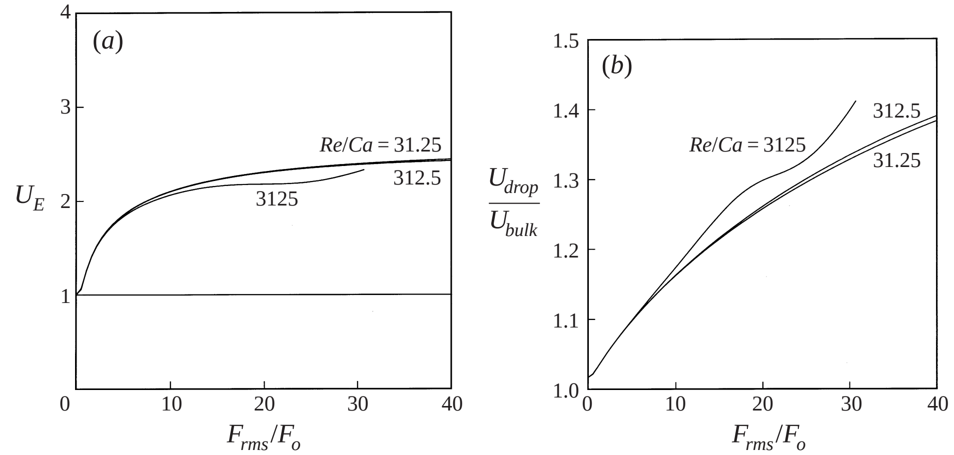

FIGURE 10. Flow rate as a function of oscillatory forcing for different Re/Ca and $a/h = 1.1$, $Ca = 5 \times 10^{-4}$, $\phi = 0.2218$, $\lambda = 1$, $\rho_D = 1$ with sinusoidal forcing: (*a*) bulk fluid, (*b*) relative drop velocity.

Re to determine when inertial effects become important. In figure 10, we show the enhancement in flow rate as a function of oscillatory forcing for three values of Re/Ca. An order of magnitude increase in Re/Ca from 31.25 to 312.5 gives an insignificant change in the flow enhancement, and further increases in Re/Ca reveal that inertial effects become significant only when the instantaneous Re reaches about 50.

5.4. *Additional parameters*

In addition to the parameters considered above, the enhancement in flow rate is a function of the droplet volume fraction, viscosity ratio and density ratio. Detailed results concerning the effects of these parameters are presented in Graham (1999). Briefly, we note that the enhancement effects increase monotonically with increasing volume fraction. This is to be expected as the greater number of droplets per unit volume increases the droplet contribution to the total pressure drop. Results for viscosity ratios ranging from $\lambda = 0.1$ to $\lambda = 10$ are qualitatively similar to those for $\lambda = 1$. The effect of increasing the density ratio ρ_D is a monotonic increase in the enhancement factor. This is consistent with the increased body force on the droplet which is proportional to its density. Note that we did not investigate effects associated with gravity forces acting perpendicular to the axis of the tube. For large density differences, such forces might lead to non-axisymmetric configurations with significant changes in the flow resistance.

5.5. *Temporal waveform*

In an effort to optimize the enhancement of the mean flow rate, we investigate the application of non-sinusoidal temporal waveforms. During sinusoidal forcing, the relatively high instantaneous fluid velocities lead to increased droplet deformation and decreased flow resistance. This decrease in resistance is advantageous during the portion of the forcing cycle in which the mean and oscillatory forcing tend to push fluid in the same direction. However, the flow resistance is also smaller when the oscillatory forcing reverses, which tends to decrease the total enhancement over the cycle. One way to optimize the enhancement is to use non-sinusoidal waveforms. In our previous work (Graham 1997), we considered a variety of temporal forcing

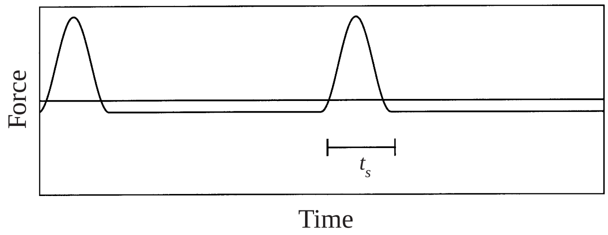

FIGURE 11. Spike waveform. The spike intervals are sine functions with a period one-fourth the overall period ($t_s/\tau = 0.25$).

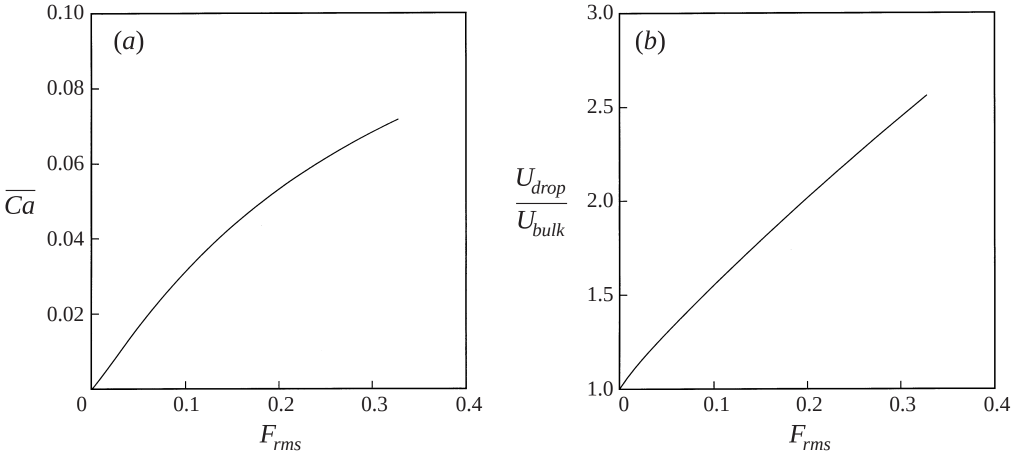

FIGURE 12. Flow rate and drop speed for spike waveform with zero mean forcing and $a/h = 1.1$, $Re/Ca = 31.25$, $\phi = 0.2218$, $\lambda = 1$, $\rho_D = 1$: (*a*) bulk fluid, (*b*) relative drop velocity.

functions, including waveforms consisting of two Fourier modes or a spike wave. A typical spike waveform is shown in figure 11 and given by

$$\left.\begin{array}{ll} 3F_\omega/4 + F_\omega \sin(8\pi t/\tau + 3\pi/2) & \text{for } t < \tau/4 \\ -F_\omega/4 & \text{for } \tau/4 > t < \tau \end{array}\right\} \tag{5.4}$$

Forcing in the positive direction consists of brief periods of strong forcing, whereas the negative portion of the forcing cycle consists of long periods of relatively weak forcing. During the portion of the cycle where the forcing is strong, the drop undergoes significant deformation and thus less flow resistance. In contrast, for the part of the cycle where the forcing is not as strong, the droplet deforms less, and therefore encounters more flow resistance. When we average over one cycle, the net result is that a mean flow is induced in the positive direction. In figure 12(*a*) we plot the average flow rate (reported as a capillary number) for the spike waveform as a function of the oscillatory forcing level in the absence of mean forcing. In figure 12(*b*) we show the ratio of drop speed to bulk velocity as a function of the oscillatory forcing level. We note that the purely oscillatory spike waveform induces a non-zero mean velocity, and that the ratio of drop velocity to bulk fluid velocity increases with oscillatory forcing.

Given that the spike waveform can induce a mean flow, we consider how the coupling of this waveform to a mean force affects the mean flow rate. Figure 13

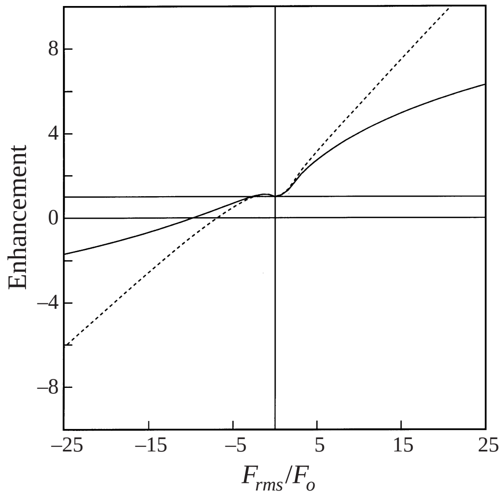

FIGURE 13. Quasi-steady analysis for spike waveform with mean forcing and $a/h = 1.1$, $Ca = 5 \times 10^{-4}$, $Re/Ca = 31.25$, $\phi = 0.2218$, $\lambda = 1$, $\rho_D = 1$. The dotted line represents the enhancement of the drop (ratio of average drop speed to drop speed without oscillatory forcing) and the solid line represents the enhancement of the bulk fluid phase (U_E).

shows the enhancement achieved for both the drop velocity (dotted line) and the bulk fluid (solid line) as a function of oscillatory forcing. In this figure, on the horizontal axis, a positive oscillatory force means that the oscillatory forcing and the mean force act to drive fluid in the same direction, whereas negative forcing means that the oscillatory component and the mean component tend to push fluid in opposite directions. For positive forcing, one sees that the acoustic forcing produces a dramatic enhancement in the mean flow rate. In contrast, negative forcing reduces the mean flow rate and may reverse the flow direction in the case of sufficiently strong forcing.

6. Unsteady flow

In the previous section we showed that quasi-steady analysis predicts a dramatic effect on the mean flow rates arising in the presence of oscillatory forcing. The quasi-steady analysis is valid for low forcing frequencies satisfying the conditions $f \ll 1$ and $f\,(Re/Ca) \ll 1$. In this section, we explore the range of frequencies over which quasi-steady predictions give reasonable approximations to the flow behaviour. We begin by examining the drop profiles in the tube and show how they are affected by the frequency of oscillation. We consider a typical flow example with sinusoidal forcing of magnitude $F_{rms}/F_o = 20$. Figures 14(*a*) and 15(*a*) show a droplet under quasi-steady flow conditions with the drop profiles showing different degrees of deformation. The small-deformation profile (figure 14*a*) illustrates the droplet in the absence of oscillatory forcing. The large-deformation profile (figure 15*a*) illustrates the maximum deformation arising in response to the oscillatory forcing. Recall that the large deformation seen in figure 15(*a*) is responsible for the lower resistance and enhanced flow rates associated with oscillatory forcing. When the frequency of oscillation departs from the quasi-steady limit ($f = 0.0088$), the drops experience some changes in deformation as shown in figures 14(*b*) and 15(*b*). Here the maximum deformation is similar to the quasi-steady limit, but the minimum deformation is greater. The oscillatory forcing produces drop elongation in the flow direction, and the droplet

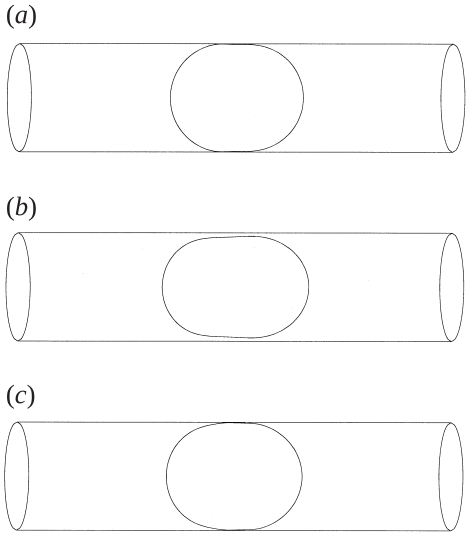

FIGURE 14. Drop shapes for $Ca = 5\times10^{-4}$, $\lambda = 1$, $\rho_D = 1$, $\phi = 0.2218$, $Re/Ca = 31.25$ corresponding to: (*a*) absence of oscillatory forcing, (*b*) the minimum deformation for $F_{rms}/F_o = 20$ and $f = 0.0088$, (*c*) $F_{rms}/F_o = 20$ and $f = 0.03168$.

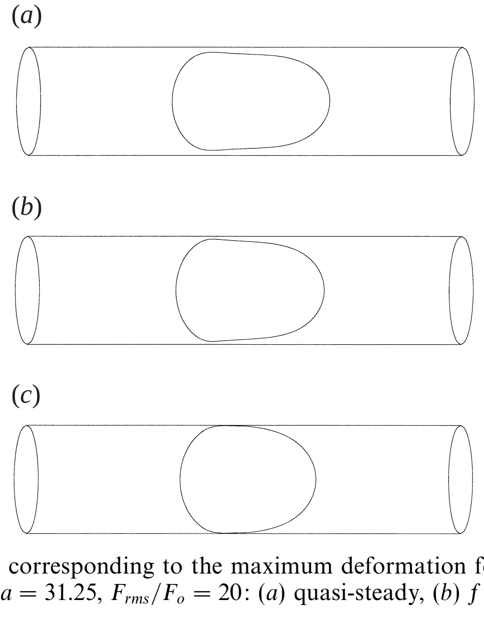

FIGURE 15. Drop shapes corresponding to the maximum deformation for $Ca = 5 \times 10^{-4}$, $\lambda = 1$, $\rho_D = 1$, $\phi = 0.2218$, $Re/Ca = 31.25$, $F_{rms}/F_o = 20$: (*a*) quasi-steady, (*b*) $f = 0.0088$, (*c*) $f = 0.03168$.

never has sufficient time to return to the less deformed state corresponding to the lowest forcing levels in the cycle. When the oscillation frequency reaches a sufficiently high value ($f = 0.03168$), the time scale for the oscillation is small enough that the droplet has insufficient time to respond to the forcing. The maximum-deformation profile shown in figure 15(*c*) shows only a minor departure from that for minimum deformation in figure 14(*c*). Each of these profiles resembles the small-deformation profile in the quasi-steady case which shows the base profile in the absence of

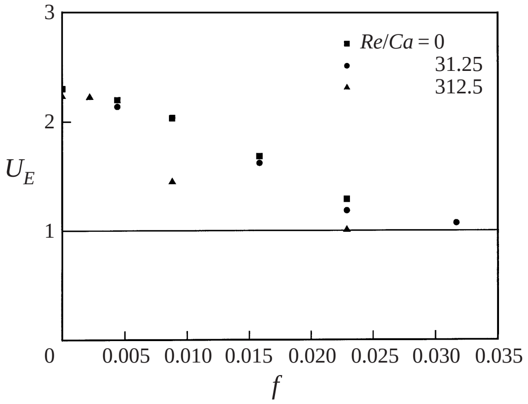

FIGURE 16. Enhancement vs. frequency for $a/h = 1.1$, $Ca = 5 \times 10^{-4}$, $\phi = 0.2218$, $\lambda = 1$, $\rho_D = 1$, $F_{rms}/F_o = 20$.

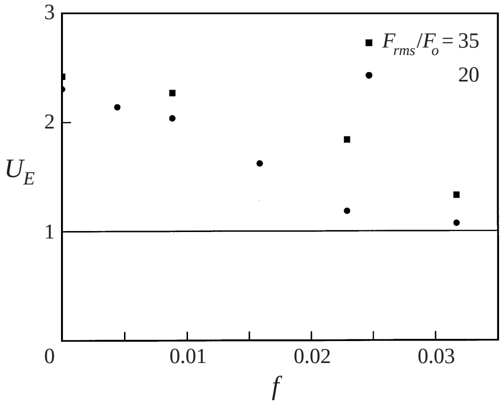

FIGURE 17. Enhancement vs. frequency for $a/h = 1.1$, $Ca = 5 \times 10^{-4}$, $\phi = 0.2218$, $\lambda = 1$, $\rho_D = 1$ and $Re/Ca = 31.25$.

oscillatory forcing. As the deformation disappears at high frequencies, the associated flow enhancement vanishes as well.

Figure 16 shows the flow enhancement as a function of frequency for three different property numbers Re/Ca. In each case, the enhancement decreases monotonically with increasing frequency. For small Re/Ca, the decay in enhancement occurs because the droplet has insufficient time to respond to the oscillatory forcing. As the property number increases however, the fall-off in enhancement shifts to lower frequencies. This shift is associated with the inertial response of the fluid. For low Re, the fluid responds immediately to an imposed force; however, for finite Re, the fluid responds more slowly owing to acceleration effects. Therefore, for the non-zero property numbers shown in figure 16, the enhancement in flow rate is limited by both the response time of the droplet and the response time of the bulk fluid. In figure 17, we show the flow rate as a function of frequency for two different oscillatory forcing levels. For both forcing levels, the flow rate decays with increasing frequency; however, the enhancement for the stronger forcing level persists at higher frequencies. For the larger forcing levels, less time is required to deform the droplet, and therefore flow enhancement remains significant for higher frequencies.

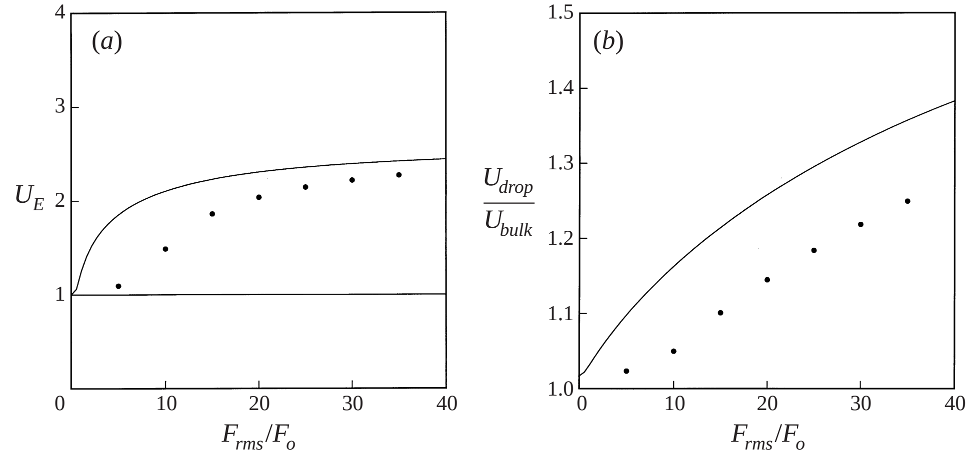

FIGURE 18. Comparison of quasi-steady prediction and unsteady simulations at $f = 0.0088$ $a/h = 1.1$, $Ca = 5 \times 10^{-4}$, $\phi = 0.2218$, $\lambda = 1$, $\rho_D = 1$, $Re/Ca = 31.25$: (*a*) bulk fluid, (*b*) relative drop velocity.

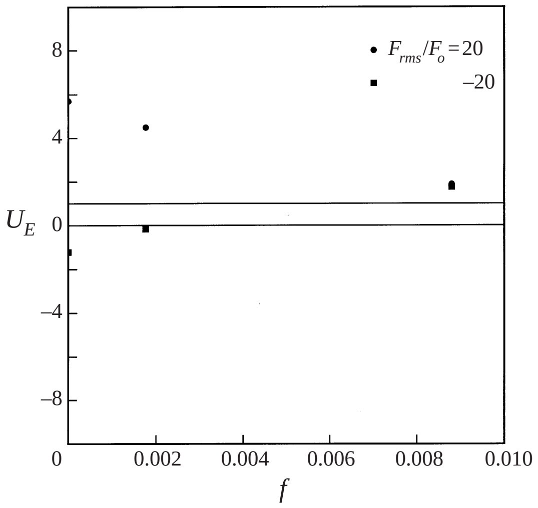

FIGURE 19. Effect of frequency on bulk fluid flow rate for spike wave and $a/h = 1.1$, $Ca = 5 \times 10^{-4}$, $Re/Ca = 31.25$, $\phi = 0.2218$, $\lambda = 1$, $\rho_D = 1$.

In figures 18(*a*) and 18(*b*), we compare the predictions of quasi-steady analysis with the unsteady simulations, plotting enhancement and drop speed as a function of forcing level for a frequency of $f = 0.0088$. The qualitative trends are the same for the quasi-steady analysis and the unsteady simulations; however there is a measurable fall-off in the magnitudes for the unsteady case. We conclude that the quasi-steady model predicts the character of the flow modification quite well over a wide range of conditions, but that attenuation at high frequency must be anticipated with figures 16 and 17 serving as a guide to the high-frequency decay.

We now move from unsteady flows driven by sinusoidal waveforms to those driven by spike waveforms. Recall that quasi-steady analysis shows that the spike wave can either increase or decrease the bulk flow rate, depending on the orientation of the forcing waveform (figure 13). Figure 19 shows the flow rate as a function of frequency for two oscillatory forcing levels with opposite orientation. For positive oscillatory forcing, the spike portion of the wave advances the fluid in the same direction as the mean. The increase in flow rate predicted by quasi-steady analysis is due to the large deformation occurring during this portion of the cycle. At higher frequencies, less deformation occurs, and therefore the mean flow rate decreases. For negative oscillatory forcing, quasi-steady theory predicts a mean flow in the direction opposite to the sense of the mean pressure gradient. This flow reversal occurs because the spike portion of the wave acts in the negative direction, yielding significant droplet deformation and reduced flow resistance for the backflow part of the cycle. As the frequency increases, less deformation occurs, and the oscillatory forcing has less effect on the mean flow rate. For the highest frequency shown, the spike portion of the wave occurs over a short enough period that the deformation change is insignificant. The slight *increase* in mean flow show in figure 19 is due to a small increase in deformation that occurs during the plateau portion of the wave. In the high-frequency asymptotic limit, the curves for both positive and negative forcing will return to the base level with no enhancement ($U_E = 1$).

7. Conclusions

We have shown that droplet deformation in response to an applied oscillatory force can lead to dramatic increases in mean flow rate for flow in straight capillary tubes. For multiphase flow in porous media, these same phenomena might lead to increased efficiency by increasing both the overall permeability of the porous media as well as the speed of the droplet phase relative to the bulk flow. The greatest enhancement is observed when strong acoustic stimulation is delivered at low frequency with large droplets and strong surface tension.

The flow enhancement observed in this study is attributable to the deformation of the fluid droplets leading to reduced flow resistance. On a macroscopic scale, this phenomenon may be characterized by viewing the suspension of droplets as an effective fluid with shear-thinning behaviour. Given the basic principles underlying the enhancement mechanism, we note that any fluid with similar rheological character would realize similar flow enhancement in the presence of an oscillatory driving force.

This work was supported by a grant from the National Science Foundation. D. R. G. acknowledges the support of a Computational Science and Engineering Fellowship from the University of Illinois. Computational resources were provided by IBM through the Shared University Resource Program at the University of Illinois, and by the National Center for Supercomputing Applications.

REFERENCES

Basaran, O. A. 1992 Nonlinear oscillations of viscous liquid drops. *J. Fluid Mech.* **241**, 169–198.

Beresnev, I. A. & Johnson, P. A. 1994 Elastic-wave stimulation of oil production: A review of methods and results. *Geophysics* **59**, 1000–1017.

Biot, M. A. 1956*a* Theory of propagation of elastic waves in a fluid-saturated porous solid. I. Low-frequency range. *J. Acoust. Soc. Am.* **28**, 168–178.

Biot, M. A. 1956*b* Theory of propagation of elastic waves in a fluid-saturated porous solid. II. Higher frequency range. *J. Acoust. Soc. Am.* **28**, 179–191.

Borhan, A. & Pallinti, J. 1998 Pressure-driven motion of drops and bubbles through cylindrical capillaries: effect of buoyancy. *Indust. Engng Chem. Res.* **37**, 3748–3759.

Bozzi, L. A., Feng, J. Q., Scott, T. C. & Pearlstein, A. J. 1997 Steady axisymmetric motion of deformable drops falling or rising through a homoviscous fluid in a tube at intermediate Reynolds number. *J. Fluid Mech.* **336**, 1–32.

Bretherton, F. P. 1961 The motion of long bubbles in tubes. *J. Fluid Mech.* **10**, 168–188.

Carnahan, B., Luther, H. A. & Wilkes, J. O. 1969 *Applied Numerical Methods*. Wiley.

Champman, A. M. & Higdon, J. J. L. 1992 Oscillatory Stokes flow in periodic porous media. *Phys. Fluids* **4**, 2099–2116.

Chapman, A. M. & Higdon, J. J. L. 1994 Effective elastic properties for a periodic bicontinuous porous medium. *J. Mech. Phys. Solids* **42**, 283–305.

Christodoulou, K. N. & Scriven, L. E. 1992 Discretization of free surface flows and other moving boundary problems. *J. Comput. Phys.* **99**, 39–55.

Coulliette, C. & Pozrikidis, C. 1998 Motion of an array of drops through a cylindrical tube. *J. Fluid Mech.* **358**, 1–28.

Davis, T. A. 1995 *Users' Guide for the Unsymmetric-pattern Multifrontal Package*. University of Florida.

Goodwin, R. T. & Schowalter, W. R. 1996 Interactions of two jets in a channel: solution multiplicity and linear stability. *J. Fluid Mech.* **313**, 55–82.

Graham, D. R. 1997 Steady and oscillatory flow through model porous media. MS thesis, University of Illinois.

Graham, D. R. 1999 Acoustic simulation of multiphase flow in porous media. PhD thesis, University of Illinois.

Graham, D. R. & Higdon, J. J. L. 2000 Acoustic stimulation of flow through porous media. Part 2. Unsteady flow. *J. Fluid Mech.* **425**, 55–77.

Gresho, P. M., Lee, R. L. & Sani, R. L. 1980 On the time-dependent solution of the incompressible Navier–Stokes equations in two and three dimensions. In *Recent Advances in Numerical Methods in Fluids* (ed. C. Taylor & K. Morgan), pp. 27–79. Pineridge Press.

Gunzburger, M. D. 1989 *Finite Element Methods for Viscous Incompressible Flows*. Academic.

Ho, B. P. & Leal, L. G. 1975 The creeping motion of liquid drops through a circular tube of comparable diameter. *J. Fluid Mech.* **71**, 361–383.

Hughes, T. J. R. 1987 *The Finite Element Method: Linear Static and Dynamic Finite Element Analysis*. Prentice-Hall.

Kheshgi, H. S. & Scriven, L. E. 1984 Penalty finite element analysis of unsteady free surface flows. In *Finite Elements in Fluids* (ed. R. H. Gallagher, J. T. Oden, O. C. Zienkiewicz, T. Kawai & M. Kawahara), pp. 393–434. John Wiley & Sons.

Martinez, M. J. & Udell, K. S. 1990 Axisymmetric creeping motion of drops through circular tubes. *J. Fluid Mech.* **210**, 565–591.

Miller, C. A. & Scriven, L. E. 1968 The oscillations of a fluid droplet immersed in another fluid. *J. Fluid Mech.* **32**, 417–435.

Muldowney, G. P. & Higdon, J. J. L. 1995 A spectral boundary element approach to three-dimensional Stokes flow. *J. Fluid Mech.* **298**, 167–192.

Olbricht, W. L. 1996 Pore-scale prototypes of multiphase flow in porous media. *Ann. Rev. Fluid. Mech.* **28**, 187–213.

Park, C.-W. & Homsy, G. M. 1984 Two-phase displacement in Hele Shaw cells: theory. *J. Fluid Mech.* **139**, 291–308.

Pozrikidis, C. 1992 The buoyancy-driven motion of a train of viscous drops within a cylindrical tube. *J. Fluid Mech.* **237**, 627–648.

Thompson, J. F., Warsi, Z. U. A. & Mastin, C. W. 1985 *Numerical Grid Generation*. Elsevier.

Tsamopoulos, J. A. & Brown, R. A. 1983 Nonlinear oscillations of inviscid drops and bubbles. *J. Fluid Mech.* **127**, 519–537.